Key Points:
- New 2-D mechanically balanced model of formation and evolution of half-grabens above low-angle normal detachment
- Tectonic extensional and gravitational modes of deformation in frictional wedges are well captured
- Fault weakening and sedimentation control number of fault-bounded blocks in hanging wall

Supporting Information:
- Supporting Information S1
- Movie S1
- Movie S2
- Movie S3
- Movie S4

Correspondence to:
X. P. Yuan,
xyuan@geologie.ens.fr

Deformation pattern during normal faulting: A sequential limit analysis

X. P. Yuan[1,2] ![ID], B. Maillot[3], and Y. M. Leroy[1,4]

[1]Laboratoire de Géologie, CNRS UMR, École Normale Supérieure, Paris, France, [2]Now at Helmholtz Centre Potsdam, German Research Center for Geosciences (GFZ), Potsdam, Germany, [3]Laboratoire Géosciences et Environnement Cergy, Université de Cergy-Pontoise, Cergy-Pontoise, France, [4]Now at Total, CSTJF, Pau, France

Abstract We model in 2-D the formation and development of half-graben faults above a low-angle normal detachment fault. The model, based on a "sequential limit analysis" accounting for mechanical equilibrium and energy dissipation, simulates the incremental deformation of a frictional, cohesive, and fluid-saturated rock wedge above the detachment. Two modes of deformation, gravitational collapse and tectonic collapse, are revealed which compare well with the results of the critical Coulomb wedge theory. We additionally show that the fault and the axial surface of the half-graben rotate as topographic subsidence increases. This progressive rotation makes some of the footwall material being sheared and entering into the hanging wall, creating a specific region called foot-to-hanging wall (FHW). The model allows introducing additional effects, such as weakening of the faults once they have slipped and sedimentation in their hanging wall. These processes are shown to control the size of the FHW region and the number of fault-bounded blocks it eventually contains. Fault weakening tends to make fault rotation more discontinuous and this results in the FHW zone containing multiple blocks of intact material separated by faults. By compensating the topographic subsidence of the half-graben, sedimentation tends to slow the fault rotation and this results in the reduction of the size of the FHW zone and of its number of fault-bounded blocks. We apply the new approach to reproduce the faults observed along a seismic line in the Southern Jeanne d'Arc Basin, Grand Banks, offshore Newfoundland. There, a single block exists in the hanging wall of the principal fault. The model explains well this situation provided that a slow sedimentation rate in the Lower Jurassic is proposed followed by an increasing rate over time as the main detachment fault was growing.

1. Introduction

Slip on low-angle detachment normal faults is suggested to occur in zones of crustal extension [*Wernicke*, 1995]. In the present paper, we develop a two-dimensional (2-D) methodology to predict the deformation pattern above a low-angle detachment fault in the brittle crust. The methodology is based on the kinematic approach of limit analysis [*Chen*, 1975; *Salençon*, 1974, 2002; *Maillot and Leroy*, 2006] developed by *Yuan et al.* [2015] to produce mechanically balanced half-graben geometrical construction.

Sites where crustal extension has produced low-angle detachments include the Gulf of Mexico [*Xiao et al.*, 1991], the northern part of the Basin and Range province (Nevada and Utah [*Anderson et al.*, 1983]), and the Corinth rift [*Rigo et al.*, 1996]. All these extensional systems are dominated by half-grabens that seem to have migrated over time. We seek here to understand the mechanisms of formation and migration of such half-grabens. *Groshong* [1989] has proposed that the hanging wall of a normal fault slides down along the fault plane and that the rocks are progressively sheared as they pass through the conjugate axial surface of the fault. *Xiao and Suppe* [1992] have complemented the half-graben kinematics description by accounting for the sedimentation that generally occurs in the hanging wall of the fault during the extensional deformation (as in the Gulf of Mexico [*Xiao et al.*, 1991] and the Albuquerque Basin [*Russell and Snelson*, 1994]). However, in these prior works, the dips of the normal faults and the axial surfaces are prescribed, not mechanically inferred. Furthermore, the half-graben migration in space during extension is not reproduced. A motivation of the present work is thus to explore the mechanics of half-graben formation and migration in extensional settings where low-angle detachments are involved.

Sandbox analogue experiments [*Xiao et al.*, 1991; *Exadaktylos et al.*, 2003] have reproduced the half-graben migration during extension. The experiments of *Dahl* [1987] revealed the existence of a region that we call foot-to-hanging wall (later referred to as FHW) where the rock material adjacent to the fault passes from the footwall to the hanging wall of the fault because of the progressive rotation of the fault as extension is going on. However, the processes and mechanisms responsible for the formation and evolution of such FHW regions are not understood yet from a mechanical point of view. Two processes, fault weakening and sedimentation, have been suggested to influence the development of faults in compressional settings [*Mary et al.*, 2013a], using the same methodology. The process of fault or slip weakening expresses the idea that faults become weaker as they slip. For this reason, these two processes are central in the modeling we perform.

Most of the present theoretical understanding of rock wedge stability above a weak detachment fault is based on the extensional Critical Coulomb Wedge (CCW) theory [*Xiao et al.*, 1991; *Yuan et al.*, 2015], which is strictly valid only for planar detachment and topographic surfaces. However, the evolution process involves internal deformation controlled by fault weakening, sedimentation, and topographic irregularities. Therefore, improved methods are required to explain the time evolution of extensional wedges. The Distinct Element Method (DEM) is well adapted to simulate the evolution of a rock wedge in extensional context, down to its small-scale fracturing. Based on this method, *Egholm et al.* [2007] indeed succeeded to reproduce the principal features of the half-graben faults including the production of narrow blocks bounded by normal faults of different dips. Heterogeneous cohesive properties could also be accounted for, and the narrow blocks were found to have a lense shape with a complex internal structure [*Schöpfer et al.*, 2007] as commonly observed. *Abe et al.* [2011] then included a fault opening mechanism at the fine scale that allowed reproducing a greater complexity of the normal faulting including some opening in the shallow crust, as observed in some analogue experiments [*Holland et al.*, 2006]. The DEM approach, however, has not yet been applied to fault evolution in extension accounting for deformation processes involving fluid pressures and fault weakening.

Therefore, we develop here a novel approach that allows modeling the space-time evolution of half-grabens while integrating weakening on the faults and that includes erosion or sedimentation processes and fluid overpressure. Few input parameters are required in this methodology: rock cohesion and friction angle, and fluid pressure. The methodology also has a small number of degrees of freedom: the dips of the two planes that bound that overall half-graben structure and the position of their common root. Therefore, it is computationally efficient, opening possibilities for inverse methods, which require a large number of forward simulations. We have indeed performed in the work presented below several thousand of simulations to fit the geometrical and material parameters of a natural fault system (Jeanne d'Arc Basin [*Withjack and Callaway* [2000]), in the spirit of the inverse analysis conducted by *Cubas et al.* [2013] for a compressional setting.

Below, we first present what is the "sequential limit analysis" for the case of a simple rock wedge above a normal detachment fault, based on the prior work by *Yuan et al.* [2015]. In section 3 we analyze a rock wedge evolution and validate the methodology. Two modes of deformation, gravitational collapse and tectonic extensional collapse, are revealed which compare well with the theoretical results of the CCW theory [*Dahlen*, 1984; *Xiao et al.*, 1991]. In subsequent section 4 we introduce additional effects, weakening of the faults once they have slipped and sedimentation in the hanging wall of the fault. We show that these effects markedly impact the results, in particular, they control the size of the FHW regions and the number of blocks they contain. Finally, we apply the new approach to restore the faults observed along a seismic line through the Southern Jeanne d'Arc Basin, Grand Banks, offshore Newfoundland [*Withjack and Callaway*, 2000] using a simplified version of an inverse method. There, a single block exists in the hanging wall of the fault. The model explains well this situation provided that the sedimentation rate has increased while the main detachment fault was growing.

The technical details of the calculations and a review of the sequential limit analysis can be found in the supporting information associated to this contribution.

2. Sequential Limit Analysis of a Homogenous Wedge Submitted to Extension

We describe here the sequential limit analysis approach through its application to a material wedge being strained on one of its lateral boundaries. The wedge (Figure 1a) is composed of a uniform and cohesive frictional Coulomb material (friction angle φ_B and cohesion C_B) and has an arbitrary topography. It is resting on an inclined, planar detachment (line *AB* with friction angle φ_D and dip β). A vertical back wall (*AC*), characterized
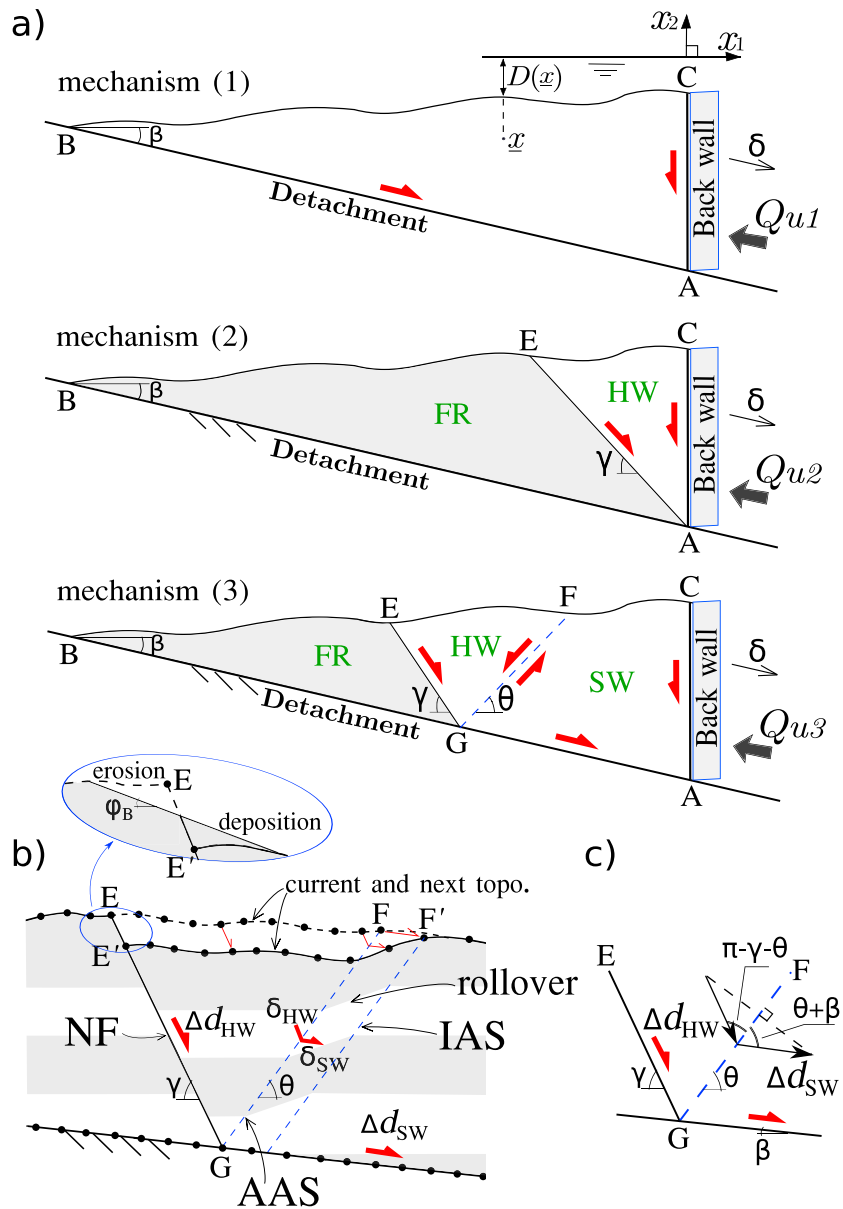
Figure 1. Upon retreat of the back wall along the detachment, (a) the wedge prototype deforms according to one of the three expected collapse mechanisms, corresponding to (1) the full activation of the detachment, (2) the activation of a normal fault *AE* rooting at the back wall, and (3) the partial activation of the detachment, of a normal fault (NF) *GE* and of an active axial surface (AAS) *GF*. HW, SW, and FR are labeled for Hanging Wall, Sliding Wall, and Frontal Region, respectively. (b) Illustration of the geometric evolution after an increment of slip for mechanism (3) based on the half-graben geometry, and illustration of erasing the fault scarp *EE'*, replaced by a slope dipping at the friction angle φ_B. In Figure 1b, the rollover is bounded by the AAS and the inactive axial surface (IAS). Grey stripes are passive markers. (c) The relation between the displacement of the hanging wall Δd_{HW} and the sliding wall Δd_{SW}, assuming mass conservation.

by the friction angle φ_{BW}, is in contact with the wedge material at its thickest side. An incremental displacement δ of the back wall parallel to the detachment and away from the wedge produces an extensional strain to the wedge/detachment system. The strain can induce three "collapse mechanisms" (Figure 1a). The first mechanism is the rigid-block sliding of the wedge along the entire length L_{AB} of the detachment fault. In the second mechanism, the detachment accommodates no displacement, and deformation therefore localizes at the back wall (Figure 1a). A third mechanism occurs when only a segment of the detachment is sliding upon the retreat of the back wall. This partial sliding, represented to occur along *AG* in Figure 1a (mechanism 3), leaves the frontal part *BEG* undeformed. A normal fault (i.e., displacement discontinuity) *GE* forms, synthetic

to the detachment. A velocity discontinuity also forms, *GF*, antithetic to the detachment. The point *G* is the "root" of the half-graben defined in between the normal fault *GE* and the active axial surface *GF* [*Xiao and Suppe*, 1992]. Note that this fault system is not symmetric by construction since the normal fault *GE* is a displacement discontinuity whereas the axial surface *GF* is a velocity discontinuity, crossed by material moving from the hanging wall to the sliding wall. Such an asymmetry corresponds to synthetic normal faulting where the fault dips in the same direction as the detachment. It is an essential feature reproduced by some experimental work [*Xiao et al.*, 1991], and it is consistent with numerical analysis [*Marshall et al.*, 2010] and field observations, such as in Brazos Ridge rollover, offshore Texas, and Mississippi Canyon and Louisiana rollovers [*Xiao and Suppe*, 1992].

The first step of the sequential limit analysis consists in determining which collapse mechanism is optimal with the help of the kinematic approach of limit analysis [*Yuan et al.*, 2015] (supporting information). The method combines the concepts of mechanical equilibrium and of energy dissipation by frictional slip along all active faults (being of Coulomb type) to provide an upper bound to the force applied at the back wall, given a collapse mechanism. The three upper bound forces at the back wall, Q_{ui}, associated to the three collapse mechanisms (*i* for mechanisms 1, 2, and 3) are thus determined and represented by thick arrows, opposite to the sliding δ of the back wall (Figure 1a). The limit analysis theorems prove that the least of the three upper bounds is associated to the mechanism the most likely to occur. This mechanism is said to be "dominant". The analytical expressions for the three bounds are given in Text S2 of the supporting information, including cases with fluid pressure. Note that the compressive forces are negative, so the minimum force corresponds to the greatest absolute compressive force. The search for the dominant mechanism requires to minimize each upper bound in terms of the geometric parameters of the corresponding mechanism: none for mechanism 1; γ for mechanism 2; and γ, θ, and L_{AG} for mechanism 3 (Figure 1a). The minimization of upper bound forces of mechanisms 2 and 3 with respect to their geometric parameters is conducted following the numerical procedure proposed by *Cubas et al.* [2008]. The detachment fault and the topography of the prototype are discretized by two sets of points (Figure 1b). For mechanism 2, upper bound forces are calculated for all discrete positions of point *E* on the top surface (defining the dip γ of the normal fault *AE*), and the least value Q_{u2} indicates the optimal dip γ. For mechanism 3, upper bound forces are calculated for all discrete positions of points *E*, *F*, *G* (defining the dips θ and γ and the length L_{AG} for mechanism 3). Again, the least upper bound Q_{u3} is associated to the optimal values of θ, γ, and L_{AG}. The dominant mechanism is the one associated to the least value among the triplet Q_{ui}.

In a second step, the sequential limit analysis updates the geometry that has changed due to the displacement δ of the back wall. For mechanism 1, the material is translated as a rigid block by the same value δ and therefore the geometry does not change. For the mechanisms 2 and 3, the geometry changes as sketched in Figure 1b ($\theta = 90°$ for mechanism 2) [*Groshong*, 1989; *Xiao and Suppe*, 1992; *Pashin and Groshong*, 1998]. We do not account for the material dilatancy, as considered by *Xiao and Suppe* [1992] and thus assume that it can be disregarded in the field, contrarily to granular materials in analogue experiments. The sliding wall (SW) and the back wall are translated by $\Delta d_{SW} = \delta$, the hanging wall slips along the normal fault *GE* by Δd_{HW}, and the frontal region is assumed to be stationary. To ensure mass conservation, the component of the displacements in the hanging wall and the sliding wall perpendicular to the axial surface *GF* should be equal to each other, i.e.,

$$\Delta d_{HW} \sin(\gamma + \theta) = \Delta d_{SW} \sin(\theta + \beta), \tag{1}$$

as illustrated in Figure 1c. The update of the system geometry and of the model topography implies that some material points of the hanging wall will cross the axial surface *GF*, as illustrated in Figure 1b. Their movement is therefore a combination of hanging wall and sliding wall displacements, δ_{HW} and δ_{SW}. Again, from mass conservation, these two displacements must satisfy the following relation

$$\frac{\delta_{HW}}{\Delta d_{HW}} + \frac{\delta_{SW}}{\Delta d_{SW}} = 1. \tag{2}$$

After their displacement, the topography points lie in the rollover zone between the active axial surface and the inactive axial surface (Figure 1b). Note that the wedge weight $\rho g S_{ABC}$, where ρ, g, and S_{ABC} are the material density, the gravity acceleration, and the wedge area, respectively, will be used to normalize the upper bound force at the back wall. This weight is constant in the absence of erosion or sedimentation.

The two steps of the sequential limit analysis described above are applied at every increment of the extension. This allows us knowing at each step which "collapse mechanism" is dominant, and documenting the evolution of the fault system as the applied extensional strain is increasing.

A surface instability might occur if the topography created in the vicinity of point E (where the normal fault intersects the topography) has a dip γ greater than the material repose angle. In this case, a surficial mass redistribution can be carried out as illustrated in Figure 1b. In this situation, we may either assume that the material has enough cohesion to sustain the steep slope without any surficial redistribution, or that the material has indeed a low cohesion (consistent with sand analogues); in this case, we replace the excessively steep slope by a slope at the repose angle set to φ_B (Figure 1b), positioned such that mass conservation is ensured [*Mary et al.*, 2013a, 2013b]. The second procedure will be adopted in section 3 where cohesionless materials are considered.

To complete this section, we need to define the fluid pressure $p(\underline{x})$ and the fluid pressure ratio $\lambda(\underline{x})$ at any point $\underline{x}$ within the wedge. We follow *Pons and Leroy* [2012] and *Yuan et al.* [2015] defining

$$\lambda(\underline{x}) = -\frac{p(\underline{x}) - \rho_f g D(\underline{x})}{\sigma(\underline{x}) + \rho_f g D(\underline{x})} \quad \text{with} \quad \sigma(\underline{x}) = \rho g(x_2 + D(\underline{x})) - \rho_f g D(\underline{x}), \tag{3}$$

where ρ_f and $D(\underline{x})$ are the fluid density and the thickness of the fluid above the saturated continuum at point $\underline{x}$ (see Figure 1a for illustration), respectively. The scalar λ in (3) varies between λ_{hydro} ($= \rho_f/\rho$) and 1, corresponding to the range from hydrostatic to lithostatic pressure. The definition of λ is crucial for the comparison with the CCW theory [*Dahlen*, 1984; *Xiao et al.*, 1991] in fluid overpressured wedges (section 3). As discussed by *Yuan et al.* [2015], the influence of the fluid pressure can be analyzed with the so-called "overpressure ratio" $\Delta\lambda = \lambda - \lambda_{hydro}$.

3. Simulation Results and Interpretation With the CCW Theory

The wedge prototype shown in Figure 1a simulates the experimental work of *Xiao et al.* [1991] with a cohesionless material and an initially flat topography ($\alpha = 0°$). Our first objective is thus to apply our numerical approach to reproduce this experiment. Numerical and analogue results will then be compared. The material and geometrical parameters (Table 1) are those given by *Xiao et al.* [1991] or, if missing, chosen consistently. Note that, as discussed in the supporting information, the normalized upper bound forces are independent of the initial detachment length for cohesionless materials. Consequently, the final shape of the structure is independent of this characteristic length. The initial detachment fault and topography are discretized into 1000 points. Extension is applied through incremental dimensionless steps $\Delta\tilde{\delta} = \Delta\delta/L_{AB}$ of 5×10^{-5}. The steps are applied until a stable wedge is obtained; from then on, further retreat of the back wall only induces a rigid slip of the wedge along the whole detachment or no displacement at all.

3.1. Numerical Results for the Case of a Dry Wedge
The evolution process is illustrated for two cases in Figures 2a and 2b where we set, respectively, a detachment dip $\beta > \varphi_D$ and $\beta < \varphi_D$. The first case for $\beta = 32° > \varphi_D$ is based on the experimental setup of *Xiao et al.* [1991]. Extension first induces deformation near the back wall (mechanism 2 at $\tilde{\delta} = 0.07$), which then extends to the central and frontal parts of the wedge by means of mechanism 3 (at $\tilde{\delta} = 0.14$ and 0.26). The simulation results match well those of *Xiao et al.* [1991]: deformation is initially observed at the back wall and then migrates toward the wedge tip as extension is increasing. Once the wedge is sufficiently thinned to reach a stable taper, it slides rigidly by mechanism 1 (Figure 2a at $\tilde{\delta} = 0.37$), no further internal deformation is registered, and the calculations are stopped. The overall deformation corresponds to a "tectonic extensional collapse" mode, defined in *Yuan et al.* [2015]; the whole topography is modified to attain a new critical shape. The critical topographic slope calculated by *Xiao et al.* [1991] is $-14.83°$, and we see that this slope is indeed that of the frontal part of the wedge (see the dashed line in Figure 2a). The surface is no longer planar in the back half of the wedge because of the influence of the rigid back wall. The cyan markers show undulations which correspond to preferred zones of activation of mechanism 3 analyzed in a later section (section 3.2).

For the case of a detachment dip $\beta < \varphi_D$ (Figure 2b), extension results essentially in a "gravitational collapse" of material near the back wall with a dominance of mechanism 2, some activation of mechanism 3 (at $\tilde{\delta} = 0.24$), and no occurrence of mechanism 1. This terminology of gravitational collapse was employed in *Yuan et al.* [2015] because of its similarity with landslides. The calculation is ended when no material remains

Table 1. Geometrical and Material Parameters for the Simulations on Wedge Prototype (Section 3)[a]

Notation	Definition	Values	Unit
α	initial topographic slope	0	degrees
β	detachment dip	20, 32	degrees
d_C	sea bed depth (Point C)	0	m
φ_a	friction angle ($a = B$, AAS, NF)	39	degrees
φ_{BW}	friction angle on back wall	30	degrees
φ_D	detachment friction angle	27	degrees
C_a	cohesion ($a = B$, AAS, NF, D)	0	Pa
ρ	saturated material density	2000	kg/m^3
ρ_f	fluid density	1000	kg/m^3
λ_{hydro}	hydrostatic pressure ratio	0.5	-
$\Delta \lambda_B$	bulk overpressure ratio	0	-
$\Delta \lambda_D$	detachment overpressure ratio	[0.0; 0.2]	-

[a]Notation: B, Bulk; AAS, Active axial surface; NF, Normal fault; BW, Back wall; and D, Detachment. Values are constant or varied within the ranges presented.

against the back wall. At this stage ($\tilde{\delta} = 0.39$), the landward dipping topographic slope matches the critical surface slope of 36.04° obtained with the CCW theory [*Dahlen*, 1984] for the gravitational collapse case. As seen from the topography and cyan markers in Figure 2, the sequential limit analysis also predicts the internal deformation necessary for the wedge to reach its stable state. We examine next the development of this internal deformation pattern.

3.2. Internal Deformation Pattern for the Case of a Dry Wedge

The evolution of the internal deformation can be better understood with the help of a *G*-gram [*Mary et al.*, 2013a], a graph showing the successive relative positions of point *G*, the common root to the normal fault and the active axial surface, with respect to the wedge tip. The dimensionless distance, $\tilde{L}_{BG} = L_{BG}/L_{AB}$ (L_{AB} the detachment length), is shown as a colored dot at each corresponding value of extension $\tilde{\delta}$ (Figure 3 with approximately five thousand extension steps). Black dots and cyan dots correspond to tectonic and gravity collapses as described in Figures 2a and 2b, respectively. Note that $\tilde{L}_{BG} = 0$ corresponds to mechanism 1 (sliding over the whole detachment), $\tilde{L}_{BG} = 1$, to mechanism 2 (back wall sliding), and $0 < \tilde{L}_{BG} < 1$ is associated with the activation of mechanism 3 (internal deformation). For the case $\beta > \varphi_D$ (black dots), mechanism 2 is active alone up to $\tilde{\delta} = 0.1$ and the dots are forming a vertical line at the right of the plot. For larger displacements, mechanism 3 starts to dominate occasionally, and both mechanisms 2 and 3 are active, up to $\tilde{\delta} = 0.369$. Stable slip with mechanism 1 finally takes over for $\tilde{\delta} \geq 0.369$ (Figure 3b). During extension with mechanism 3, the *G* points are organized in a series of eight V's developing toward the wedge tip. The spacing between the various V's is such that the active axial surface of a given half-graben intersects the topography close to where the normal fault of the neighboring half-graben does. There is also some minor activity, with similar V structure but more diffuse, inside the main eight V's. This *G*-gram structure is reminiscent of the one found in compressional settings by *Mary et al.* [2013a, 2013b] where forethrusts are grouped along the detachment such that the topography tends toward a straight line at the critical slope. Here at least eight V's develop over the detachment ensuring thinning of the wedge with the final critical surface slope. This distribution of V's results in a nonuniform deformation, with relatively undeformed regions separated by highly sheared zones as is observed in the undulations of the markers in Figure 2a. The V's are induced from back wall to wedge tip and cease their activity also from the back wall to front tip, as seen from the decreasing density of points in each V as the wedge is getting closer to stable slip (Figure 3b).

In contrast, for case $\beta < \varphi_D$ (cyan dots), mechanism 2 is active throughout extension but is combined with mechanism 3 for $\tilde{\delta} \geq 0.2$. Mechanism 3 develops three similar (but with a mirror symmetry) V patterns in the *G*-gram, with a reverse spatial evolution, from wedge tip to the back wall.
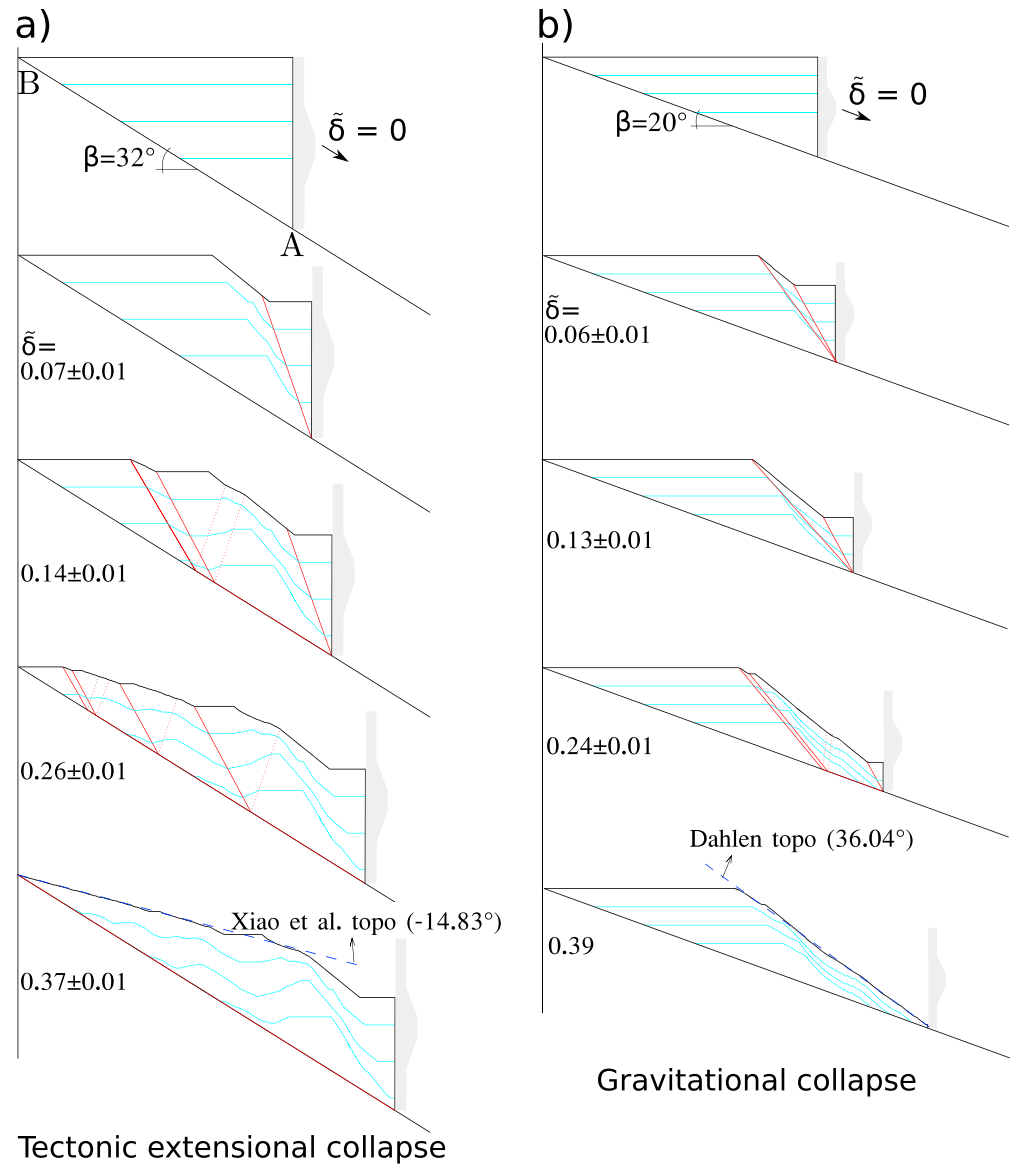
Figure 2. The extension results in either a tectonic extensional collapse, (a) $\beta = 32° > \varphi_D$, or in a gravitational collapse for (b) $\beta = 20° < \varphi_D$. Solid and dotted red lines represent, respectively, normal faults and active axial surfaces during the three displacement steps around the displacement value $\tilde{\delta}$ indicated in each plot. Cyan lines are passive markers revealing internal deformation. Dry conditions are considered. Animation of the numerical experiment for Figure 2a is presented in the supporting information. Vertical and horizontal scales are equal. See Table 1 for parameter values.

3.3. Numerical Results for the Case of an Overpressured Wedge

We now illustrate how fluid overpressure on the detachment may change the mode of extension of the wedge from gravitational to tectonic collapse. The fluid overpressure ratio $\Delta\lambda_D$ in the detachment is varied within the interval [0.0; 0.2], and hydrostatic conditions are considered in the bulk material ($\Delta\lambda_B = 0$). Only final geometries obtained for $\beta = 20° < \varphi_D$ are presented in Figure 4. Without overpressure on the detachment, the final geometry is that of Figure 2b. For increasing overpressure $\Delta\lambda_D$ up to 0.1, the gravitational collapse mode still dominates but the final topographic slope decreases because the overpressure reduces the mechanical strength of the detachment. The change in mode of deformation from gravitational to tectonic extensional collapse occurs for $\Delta\lambda_D$ between 0.10 and 0.15. The two cases of $\Delta\lambda_D = 0.15$ and 0.20 are thus of a tectonic extensional collapse mode. Note that a stable wedge is reached for less extension when overpressure is greater. This is a consequence of the decrease in the CCW topographic slope with increasing $\Delta\lambda_D$ in the tectonic extension mode. Note also that all final geometries presented in Figure 4 exhibit a topographic slope
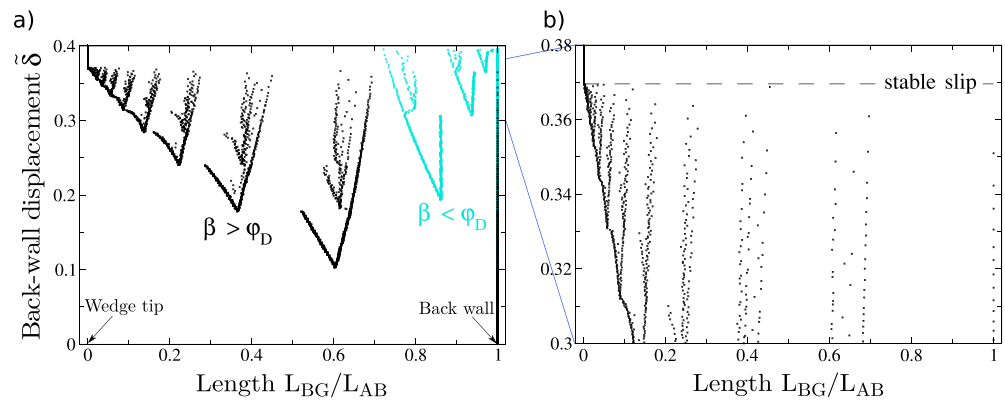
Figure 3. The *G*-gram presents the position of the common root of the normal fault and the active axial surface (point *G*, Figure 1a) for increasing back wall dimensionless displacement (vertical axis). (a) Black dots ($\beta > \varphi_D$) and cyan dots ($\beta < \varphi_D$) correspond to the evolution processes in Figures 2a and 2b, respectively. (b) A close up on the *G*-gram for the case $\beta > \varphi_D$ only, showing the gradual transfer of internal deformation toward the wedge tip for $\tilde{\delta} \leq 0.369$ and the switch to stable sliding ($L_{BG}/L_{AB} = 0$) for $\tilde{\delta} > 0.369$.

which matches quite well the critical slope of the CCW theory, once properly amended by *Wang et al.* [2006] (called ECCW (E for exact) theory in *Yuan et al.* [2015]).

The match between the computed wedge topography and the critical slope predicted with the CCW theory validates the sequential limit analysis and our choice of collapse mechanisms (Figure 1a). It constitutes also a nontrivial verification of our numerical implementation.

4. Roles of Fault Weakening and of Sedimentation

The objective is now to concentrate on the hanging wall of the normal fault and to study the effects of sedimentation and fault weakening on its deformation. Fault weakening refers to the fact that faults are planes of frictional weakness compared to the bulk material (lower friction angle and/or cohesion). Various processes can lead to fault weakening such as slip weakening at the earthquake dynamic scale or clay smearing or smoothing at longer timescales. In our simulations, we set the prescribed weakened properties to any fault after it has sustained a first slip increment. In doing so, we do not refer to any specific weakening process.

We use a new prototype shown in Figure 5a that contains a lower normal fault (segment *AG*) not extending to the surface and playing the role of detachment fault. This detachment is buried at depth *h* beneath the initially flat topography. To analyze the deformation of the wedge, we refer here to a mechanism 4 (Figure 5b), which includes slip along the normal fault *GE* rooting at the upper end of the detachment (point *G*). Mechanism 4 is identical to mechanism 3 presented in Figure 1a except for two differences. First, the position of point *G* is predetermined, and second, the normal fault *GE* (dipping at an angle γ) has specific material properties in order to describe its possible weakening. The active axial surface *GF* rooting at point *G* is dipping at θ. These two dips γ and θ are optimized according to the limit analysis discussed in section 2. The expression for the upper bound force at the back wall is given in Text S3 of the supporting information. Material parameters are given in Table 2. Weakening of the normal fault *GE* is implemented as follows: the friction angle of the fault is set to the bulk friction φ_B if the fault has not slipped in the previous step. By contrast, if the fault has slipped in the previous deformation step, we decrease its friction angle value to φ_{NFW} (NFW: normal fault with weakening). This is a simplified version of the linear weakening law considered in *Cubas et al.* [2008]. Of course, when the value of φ_{NFW} is equal to φ_B, there is no fault weakening. Note that no weakening memory is accounted for once the weakened fault stops slipping, fault healing is instantaneous, i.e., the friction angle is restored to its original bulk value.

To ensure that the deformation occurs by activation of the detachment fault and not by a gravitational collapse at the back wall, we refer again to the extensional CCW theory [*Xiao et al.*, 1991], Figure 6a. The stability domain of the extensional CCW theory is plotted for two values of the detachment friction angle $\varphi_D = 10°$ and 30°. For a prototype with (β, α) outside this stability domain, the collapse characterized by the deformation near the back wall (e.g., the mechanism 2 in Figure 1a) is expected. To the contrary, within the grey stable domain, the deformation should be controlled by slip on the detachment and complemented
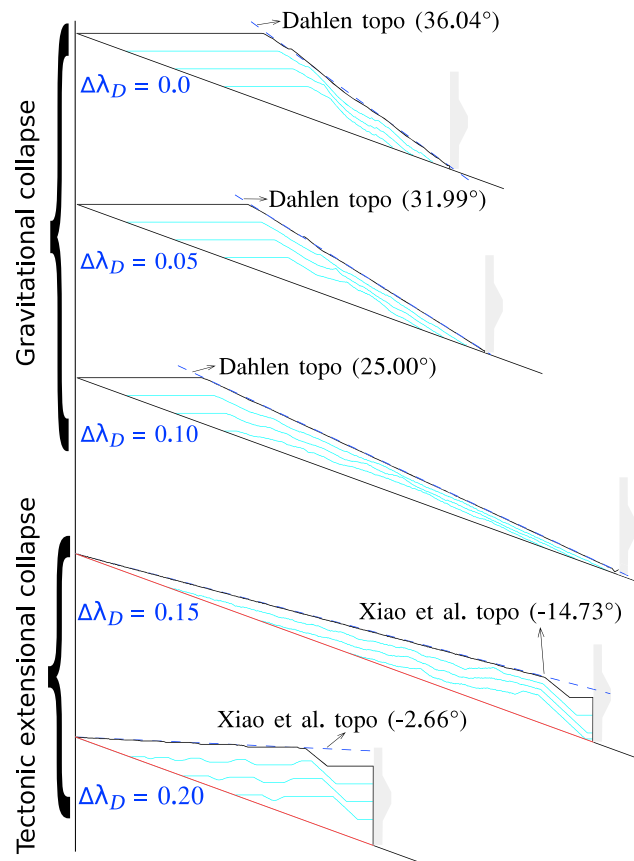
Figure 4. Stable wedges in various detachment overpressure ratios $\Delta \lambda_D$. Detachment dip is $\beta = 20°$, and the back wall friction angle is $\varphi_{BW} = 30°$. See Table 1 for other parameters. The blue dashed lines correspond to the critical slopes calculated from *Dahlen* [1984] or from *Xiao et al.* [1991], with the ECCW theory in *Yuan et al.* [2015] for fluid overpressured cases. Vertical and horizontal scales are equal.

Table 2. Geometrical and Material Parameters for the Simulations of the Hanging Wall Deformation in Sections 4 and 5[a]

		Values		
Notation	Definition	(Section 4)	(Section 5)	Unit
α	initial topographic slope	0	0	degrees
β	detachment dip	30, 45, 60	18	degrees
h	cover thickness	0.3	12×10^3	m
d_D	sea bed depth (Point D)	-	0	m
φ_a	friction angle ($a = B$, AAS)	32	35	degrees
φ_{NFW}	NF friction angle with weakening	25, 30, 32	[20; 34]	degrees
φ_D	detachment friction angle	10, 30	10	degrees
C_a	cohesion ($a = B$, AAS, NF, D)	0	0	Pa
r_S	sedimentation ratio	[0.0; 1.4]	variable	-
ρ	saturated material density	2000	2500	kg/m^3
ρ_f	fluid density	-	1000	kg/m^3
λ_{hydro}	hydrostatic pressure ratio	-	0.4	-
$\Delta \lambda_B$	bulk overpressure ratio	-	0	-
$\Delta \lambda_D$	detachment overpressure ratio	-	0.2	-

[a]Notation: B, Bulk; AAS, Active axial surface; NF, Normal fault; and D, Detachment.
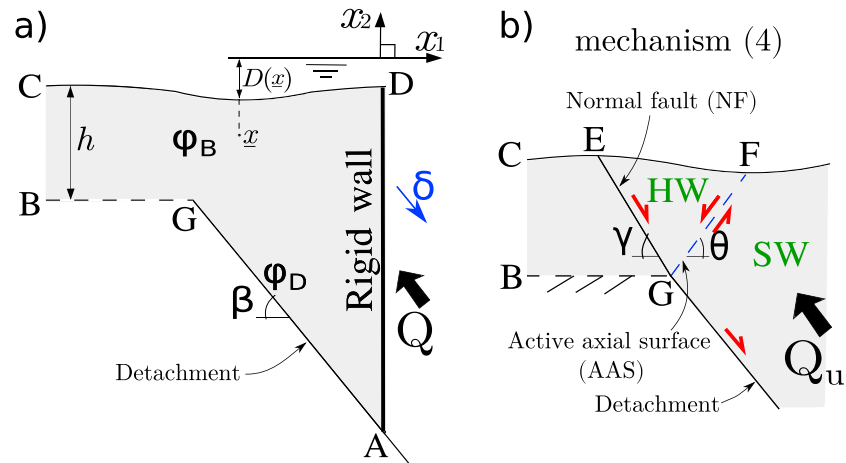
Figure 5. (a) The prototype considered in sections 4 and 5 consists of a detachment fault *AG* and an initially flat cover. (b) The collapse mechanism 4 composed of a normal fault and an active axial surface rooting at point *G* and is identical to mechanism 3 (Figure 1a), except that point *G* is fixed.

by an upper normal fault as in mechanism 4. Consider now the detachment fault dips of 30°, 45°, and 60° corresponding to the three blue squares in Figure 6a. They are aligned on the horizontal line $\alpha = 0°$ corresponding to the initially flat topography. The case of $\beta = 60°$ is within the two stability domains and thus the whole detachment should be activated regardless of the two values of the detachment friction angle. For a dip β equal to 30° and 45°, the activation of the detachment should only occur for the friction angle φ_D of 10°. For the larger value of 15°, deformation should initiate near the back wall, as illustrated in Figure 6a, prior to the propagation of the detachment fault through the cover. This transition of the deformation activity from the back wall to the wedge tip was discussed in the previous section and will be disregarded in what follows since only mechanism 4 in Figure 5b is applied.

4.1. Reference Simulations

As a reference, we present in Figure 7 six simulations without fault weakening nor sedimentation and set β to 30°, 45°, or 60°, φ_D to 10° or 30°, and imposing a small back wall displacement $\tilde{\delta} = 0.2$ parallel to the detachment (displacement is normalized by the thickness *h* of the initial cover: $\tilde{\delta} = \delta/h$). Note that the normal fault dip γ is greater than β so the overall normal fault *AGE* is concave, except for case f where $\gamma \approx \beta$. Hanging wall material is sheared when crossing the active axial surface and entering into the rollover domain (Figure 7d). The inactive axial surface IAS was the first active axial surface AAS and is now translated by the downward displacement (Figure 7d). Material in the rollover is thinned and has an antithetic dip. Rollovers are commonly observed in the field and were described with geometrical models [*Xiao and Suppe*, 1992]. We find here a mechanical justification and a quantitative link between the geometrical models and the frictional properties.
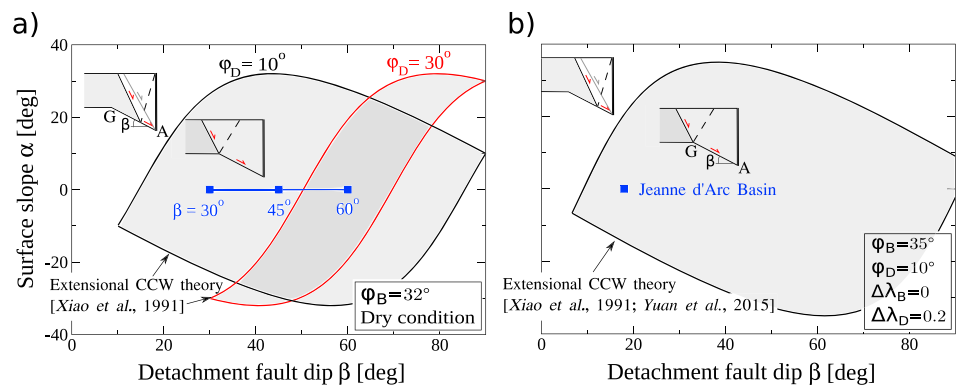

Figure 6. The stability domain of the extensional CCW theory [*Xiao et al.*, 1991; *Yuan et al.*, 2015] is used to check that the initial states for the simulations in (a) section 4 and the application in (b) section 5, correspond to the activation of the detachment *AG* rather than to a collapse occurring near the back wall.
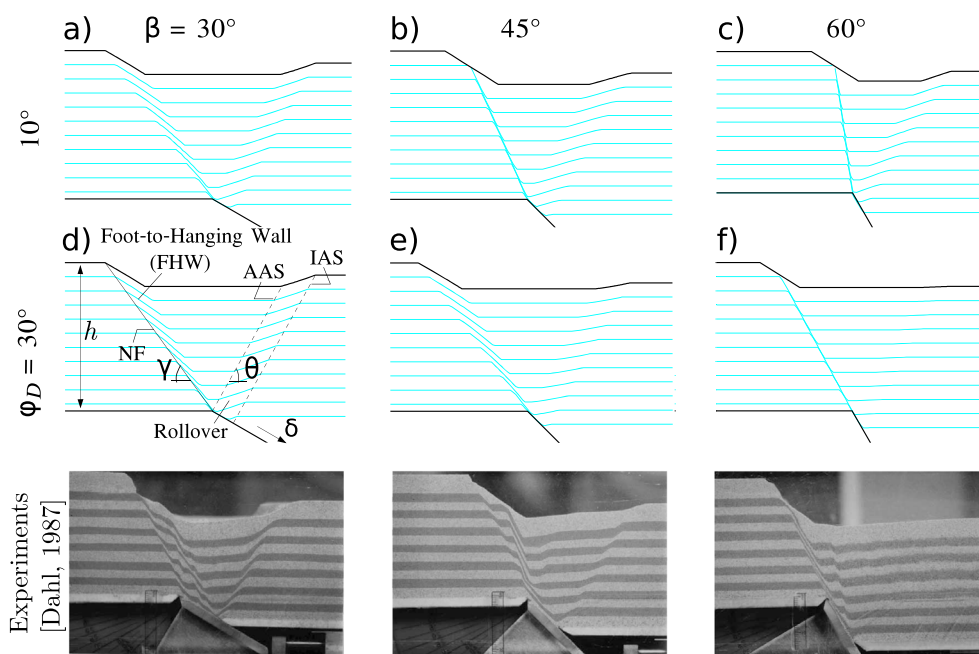
Figure 7. Six simulations are presented ignoring the effects of fault weakening and sedimentation. The detachment dips are at (first column) 30°, (second column) 45°, or (third column) 60°, and the associated friction angle φ_D is set to (first row) 10° or (second row) 30°. (third row) Analogue experiments from *Dahl* [1987] and *Egholm et al.* [2007] with $\beta = 30°$, 45°, and 60°. In Figure 7d, the oblique solid line indicates the current active normal fault (NF), while the dashed lines represent the active axial surface (AAS) and the inactive axial surface (IAS). Vertical and horizontal scales are equal.

In case f, the detachment has a friction $\varphi_D = 30°$ close to the bulk friction $\varphi_B = 32°$ and a dip $\beta = 60°$ near the Andersonian dip $\pi/2 - (\pi/4 - \varphi_B/2) = 61°$. The sequential limit analysis optimization then yields $\gamma \approx \beta$ as expected from Anderson's theory, and there is no rollover because the axial surface does not play the role of a velocity discontinuity between the hanging and the sliding walls.

The sequential limit analysis can include another effect that is generally ignored in geometrical constructions: the change in dip of the normal fault as the hanging wall subsides. For a large detachment friction angle φ_D (cases d and e) and for a low detachment dip (case a) in Figure 7, the dip γ decreases approximately by 10° with ongoing displacement while the dip θ of the axial surface remains approximately constant. This rotation produces a triangular region where the material sustains intense shear. This region is referred to as the foot-to-hanging wall (FHW) region, because its material was originally in the footwall below the active normal fault, and is now in its hanging wall. The physical interpretation of the rotation of the active normal fault is far from being obvious, at least for the authors, and we first rely on an inspection of the governing equations (S9) and (S10) in the supporting information as well as the hodogram in Figure S4a which provides the geometric interpretation of equation (S9). From equation (S10), it appears that, in the absence of cohesion and fluid overpressure, the minimum force is controlled by the power of the gravity force on the sliding wall and on the hanging wall velocities. The former contribution is increasing linearly with extension because the axial surface dip remains constant to first order regardless of the value of γ. The latter term results from the product of three components: the current area of the hanging wall, its velocity norm and a scalar due to the projection of the velocity on the direction of the gravity action, and the vertical axis. Reducing γ increases the hanging wall area and increases the velocity norm, as seen from Figure S4a, but reduces the scalar due to the projection. Physically, the interpretation is that reducing γ increases the material area involved in sliding as well as the sliding velocity norm (decreasing the tectonic force) but reduces the action of gravity (increasing the tectonic force). It is the balance of these three influences which control the normal-fault rotation during the topographic subsidence.

A number of features observed in sandbox experiments including the production of FHW regions [*Dahl*, 1987; *Egholm et al.*, 2007], shown in Figure 7 (third row), are clearly replicated by our simulations. Observed rollovers develop for $\beta = 30°$, 45°, but not for $\beta = 60°$, and FHW regions are observed for all three cases $\beta = 30°$, 45°, and 60°, like in our simulations. For $\beta = 45°$ and 60°, the fault rotation has occurred suddenly, creating
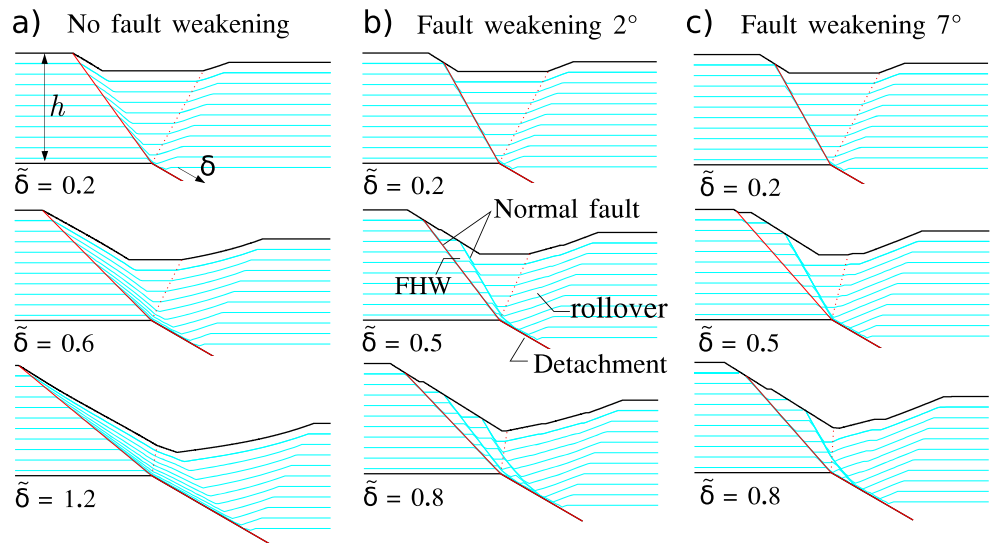
Figure 8. Effect of weakening of the normal fault. The evolution process for (a) no fault weakening, (b) 2°, and (c) 7° drop of the normal fault friction angle, for various values of $\tilde{\delta} = \delta/h$ (slip on the detachment over the cover thickness). In Figures 8b and 8c, surface is deflected across the faults but not offset because of surface process (erosion and deposition), illustrated in Figure 1b. Vertical and horizontal scales are equal.

undeformed conical blocks in the FHW, and this has not occurred in our simulations where a continuous rotation takes place instead. This motivates the introduction of fault weakening into the modeling.

4.2. Fault Weakening

The simulation results for $\beta = 30°$ and $\varphi_D = 30°$ are selected in this subsection because they produce a rather large FHW region (Figure 7d). This configuration is ideal to introduce a further complexity in the model: fault weakening. We recall that any new normal fault has a friction equal to the bulk friction φ_B, whereas a reduced friction angle φ_{NFW} (for normal fault with weakening) is assigned to the fault once it has sustained its first increment of displacement. No memory is kept of the fault weakening once the fault is deactivated.

The simulation without fault weakening (Figure 7d) is prolonged to $\tilde{\delta} = 1.2$ (Figure 8a), and simulations with 2° fault weakening ($\varphi_{NFW} = \varphi_B - 2° = 30°$) and 7° ($\varphi_{NFW} = 25°$) are shown in Figures 8b and 8c, respectively. These series of plots show that the normal fault progressively rotates counterclockwise up to having a dip close to β. This evolution and the dip changes of the normal fault and the active axial surface are presented in Figure 9. The variation of γ appears to be gradual, increasing the area of the FHW region. The total volume of the cross sections is conserved because there is no external sedimentation. At the same time, the active axial surface also rotates counterclockwise up to approximately 80° (solid black curve (θ) in Figure 9) producing a slight curvature in the rollover beds (Figure 8a). The dip θ of the active axial surface reaches a roughly constant value when all the flat beds initially in the hanging wall have passed through the active axial surface (Figure 9 for $\tilde{\delta}$ larger than 0.86, approximately).

In Figure 8a ($\tilde{\delta} = 1.2$), the material of the FHW region keeps a synthetic dip. The cases with fault weakening (Figures 8b and 8c) also show rotation of normal faults and active axial surfaces, but the rotation is now stepwise (Figure 9, blue and grey lines). The rotations of the normal fault and of the active axial surface occur simultaneously. The sudden weakening on the active normal fault implies a sharp drop in the corresponding upper bound of the compressive force at the back wall and thus the possibility to remain active during a finite period of extension. The resulting finite deformation is markedly different from the case without weakening, with the FHW region being dissected by several fault-bounded blocks instead of being a continuous shear zone. Note also that a single block or two blocks are produced, depending on the amount of weakening (Figures 8b and 8c at $\tilde{\delta} = 0.8$). In the rollover region, the jump in dip of the active axial surface (at $\tilde{\delta} = 0.39$) resulted in a kink band, visible at $\tilde{\delta} = 0.5$ and 0.8 in Figure 8c.

With this new insight we can look again at the analogue experiments in Figure 7 in which the FHW regions are composed of one or several fault-bounded blocks. Our simulation results suggest that weakening of the sand analogue material might be an explanation to the development of these structural features (with sand,
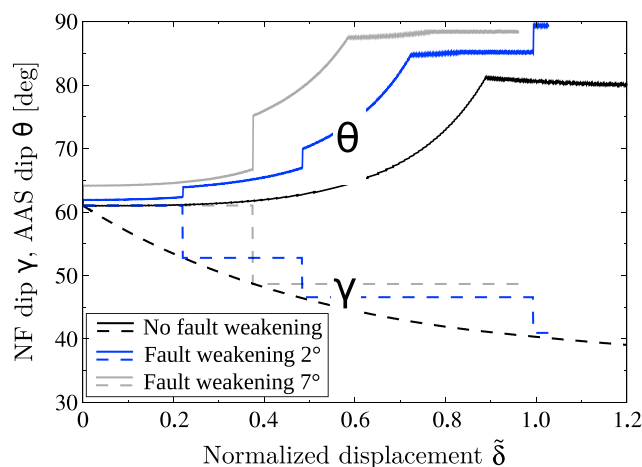
Figure 9. Variations of the dip of the normal fault (γ, dashed curves) and the dip of the active axial surface (θ, solid curves) with displacement $\tilde{\delta}$, for the three fault weakening cases in Figure 8.

weakening is essentially function of the initial density of the pack, and therefore to grain size distribution and handling technique, and corresponds to a dilatation along the fault plane that allows grains to roll pass each other when the fault is fully formed [*Lohrmann et al.*, 2003; *Panien et al.*, 2006; *Maillot*, 2013]. Moreover, a moderate fault weakening produces many jumps which might not be distinguishable from the continuous rotation. It is only for a fault weakening greater than 2° that the number of blocks becomes observable. For even larger fault weakening values, the number of jumps in dips decreases and the number of blocks is reduced for the same extension. We see next that the sedimentation stabilizes the rotations of the normal fault and of the active axial surface and affects the number of blocks in the FHW region.

4.3. Sedimentation and No Fault Weakening

Sedimentation is modeled by filling the topographic depression formed in the hanging wall with material of the same physical properties as the pregrowth strata. The compaction of sediments is not considered. The thickness Δh_S of sedimentation is calculated such that the sedimentation ratio defined by *Xiao and Suppe* [1992], $r_S = \Delta h_S / (\Delta d_{HW} \sin \gamma)$, as the sedimentation increment to the hanging wall subsidence increment, is a constant. Note that the rotation of the normal fault leads to the variation in $\sin(\gamma)$ during extension and thus Δh_S is not a constant.

The consequence of selecting r_S smaller than, equal to, or greater than 1 can be foreseen. A hanging wall depression is formed when the sedimentation ratio r_S is smaller than 1 with the consequence on the normal fault rotation discussed above. For a ratio $r_S = 1$, the original flat topography is preserved during extension. A ratio $r_S > 1$ means that the elevation of the flat topography is increasing during extension.

The simulation with no fault weakening of Figure 8a is now repeated with a constant sedimentation ratio for each simulation. This ratio r_S varies from 0 to 1.4, and the final extensional displacement is $\tilde{\delta}_f = 1.1$. Results are presented in Figure 10 and the growth strata are represented by four black markers (one every $\tilde{\delta}_f/4$). The first observation is that an increase in the sedimentation rate reduces the counterclockwise rotation of the normal fault and of its associated active axial surface. This is because sedimentation reduces the formation of topographic gradients. As a consequence, at high sedimentation ratio, the FHW region may be very small or may not occur at all. This effect is seen for $r_S \geq 1$, in which the simulation results match the geometrical models of *Xiao and Suppe* [1992]: the dips of the normal fault and of the active axial surface are constant, see Figure S5 in the supporting information. Animations of the numerical experiments for $r_S = 0.0, 0.6$ and 1.4 are also presented in the supporting information.

Our simulation results have four features similar to those of the geometrical constructions of *Xiao and Suppe* [1992], Figure S5 in the supporting information. First, the thicknesses of the syntectonic sediments vary between the footwall, the hanging wall, and the sliding wall, and those variations are similar in the geometrical constructions and in our mechanical constructions. Second, the rollover is now composed of the pregrowth material and new, syntectonic sediments (if $r_S > 0$). Third, the top of the rollover, called the growth axial surface [*Xiao and Suppe*, 1992] and labeled as such in Figure 10, indeed separates syntectonic sediments with
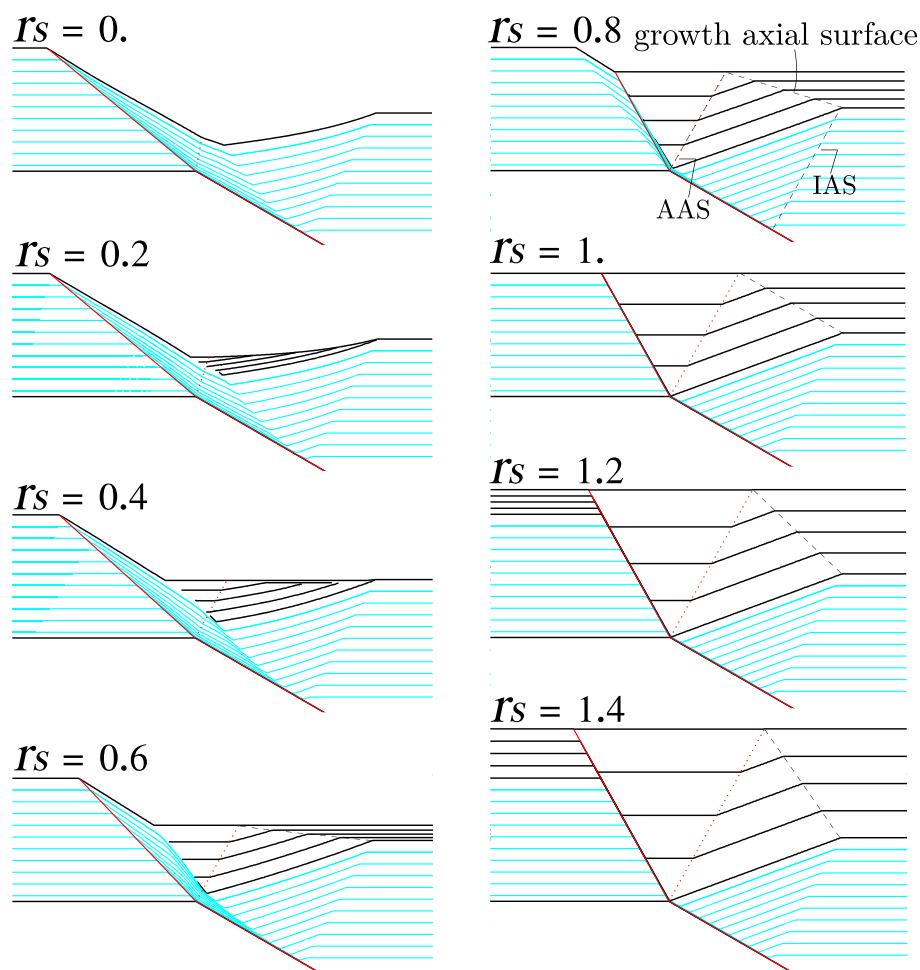
Figure 10. Influence of an increase in the sedimentation ratio r_S on the hanging wall deformation pattern. The conditions are the same as in Figure 8a (no fault weakening). The cyan markers are pregrowth strata, whereas the black markers correspond to the growth strata. The final displacement for all calculations is $\tilde{\delta}_f = 1.1$. Vertical and horizontal scales are equal.

or without shearing through the axial surfaces. Fourth, the dip of the growth axial surface increases with the sedimentation ratio r_S.

4.4. Combined Effects of Sedimentation and Fault Weakening

The objective is now to combine the effects of fault weakening and sedimentation to shed light on the hanging wall deformation pattern. A ratio r_S less than 1 is considered since for $r_S \geq 1$ the deformation pattern is relatively simple without rotation of the normal fault and of the active axial surface. An additional effect is considered, the role of a local surficial mass redistribution. The sediment mass is either redistributed, such that the topographic slope never exceeds the repose angle (equal to the bulk friction angle), or the sediments have enough cohesion so that the fault offset of the topography is preserved.

Results presented in Figure 11 (left column) are for 2° fault weakening with surficial mass transport, whereas those in Figure 11 (right column) ignore the effects of mass redistribution. We observe that sedimentation efficiently stabilizes the rotation of the normal fault and of the active axial surface in the presence of weakening (compare the results for $r_S = 0.8$ in Figures 10 and 11). Increasing the sedimentation rate reduces the number of blocks in the FHW region. There are two blocks for $r_S \leq 0.4$ and only one block for $r_S = 0.6$ for 2° fault weakening. A comparison of the two columns of Figure 11 shows that the surficial mass transport has similar effects to those of sedimentation: it reduces the rotation of the normal fault and of the active axial surface and reduces the number of blocks within the FHW region. There is only one block for $r_S = 0.4$, whereas there are two blocks for the case without mass redistribution.
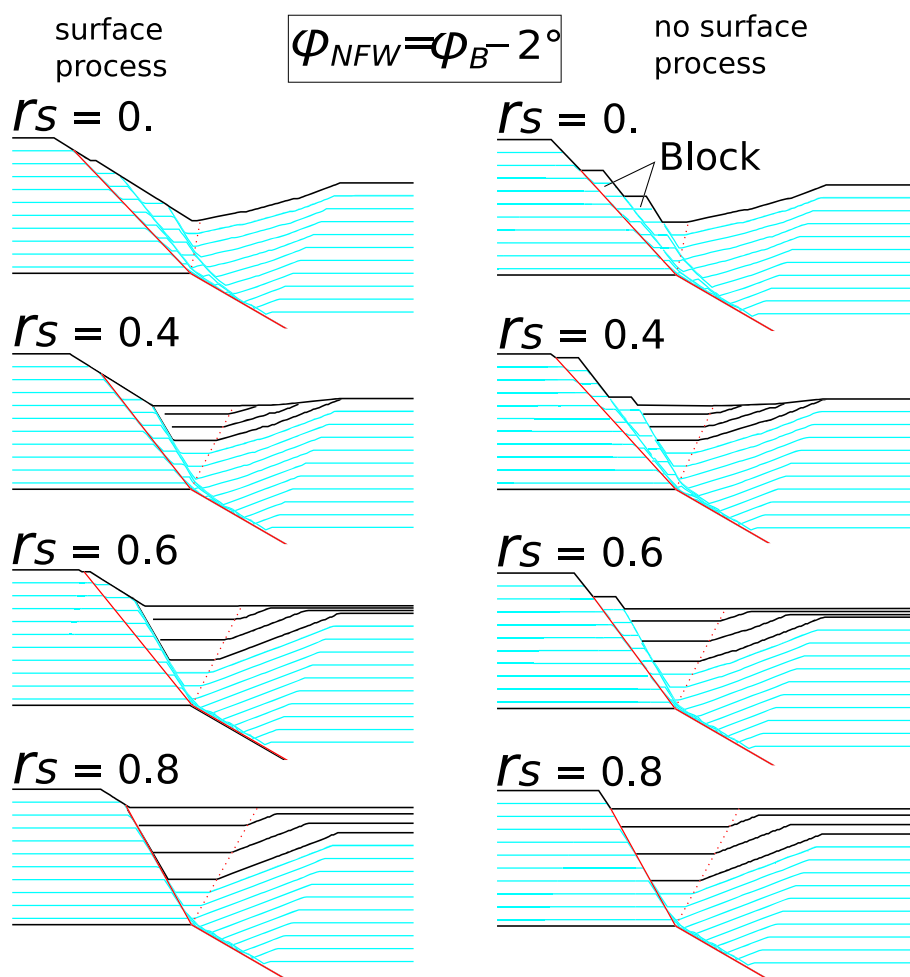
Figure 11. Combined effects of sedimentation and of fault weakening (2°) on the hanging wall deformation pattern. (left column) The oversteepened surface fails essentially by landsliding, erasing the fault scarp. The slope cannot exceed the repose angle. (right column) The fault scarp is not modified. The final displacement for all calculations is $\tilde{\delta}_f = 0.8$. Vertical and horizontal scales are equal.

Consider now the case of 7° weakening shown in Figure 12 and compare with the case of 2° fault weakening. For larger weakening, the sedimentation effect on the rotation of faults is even stronger and is now effective for $r_S \geq 0.6$ instead of 0.8 previously. The earlier observation that large weakening reduces the number of blocks in the FHW region is confirmed in the presence of sedimentation ($r_S \geq 0.4$). Comparing now the two columns of Figure 12, it is observed as before that the surficial mass transport is important for intermediate sedimentation ratio around 0.4.

In summary, described with the sequential limit analysis, the collapse mechanism 4 (Figure 5b) links the dips (γ, θ) of the geometrical models of *Xiao and Suppe* [1992] to material and fault properties and to the topographic evolution due either to sedimentation or surficial mass redistribution. In some cases, the classical assumption of constant dips is confirmed by the optimization (important fault weakening and/or sedimentation), at the Andersonian dip value of 61° ($\pi/4 + \varphi_B/2$). In the other cases, γ and θ evolve substantially, producing important differences such as the FHW region with or without fault-bounded blocks, or smaller differences, such as perturbations in the dips found in the rollover region. We now apply our new approach to examine the formation of a natural sedimentary basin.

5. Application to Jeanne d'Arc Basin, Grand Banks, Newfoundland

This section is devoted to a parametric study of the mechanical properties and the field conditions (sedimentation ratio r_S) which might have prevailed during the development of a natural half-graben. The half-graben
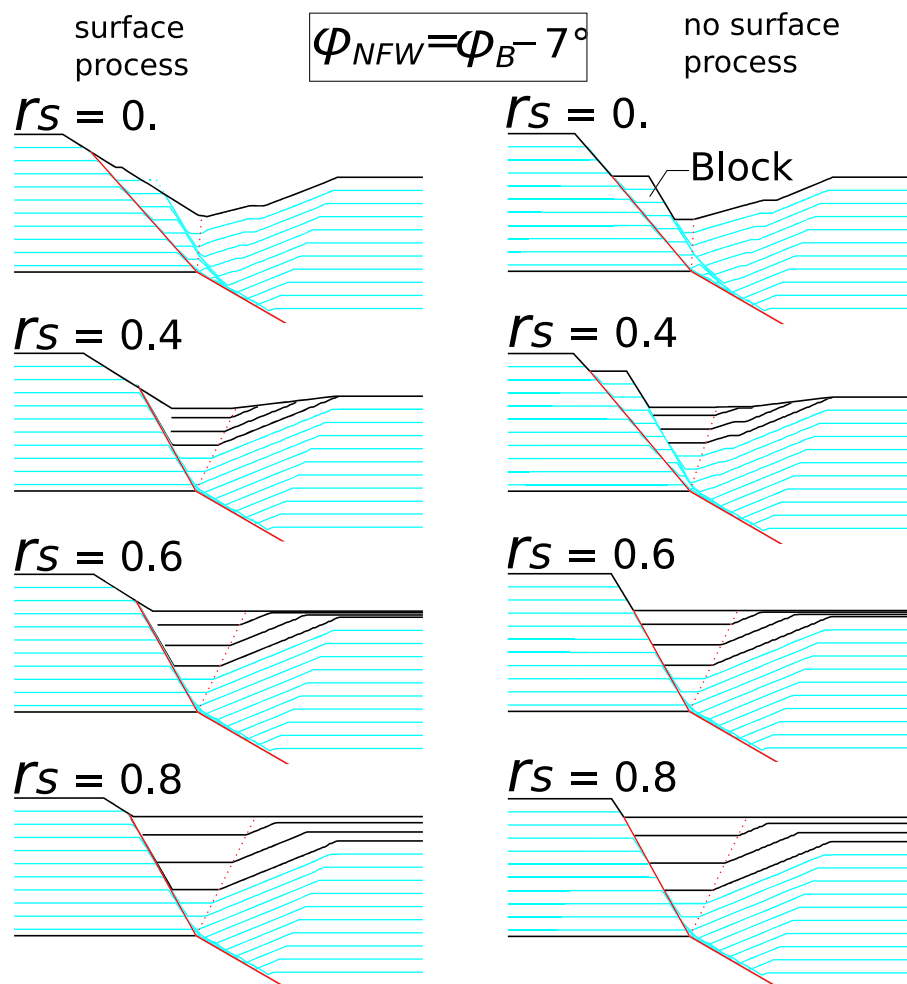
Figure 12. Combined effects of sedimentation and of fault weakening (7°) on the hanging wall deformation pattern. (left column) Results with surface process (slope cannot exceed repose angle) for cohesionless materials. (right column) Results that do not have the surface process. The final displacement for all calculations is $\tilde{\delta}_f = 0.8$. Vertical and horizontal scales are equal.

is located in the Jeanne d'Arc Basin, Grand Banks, Newfoundland. Its faults are imaged on a deep seismic reflection profile 85-4A [*Withjack and Callaway*, 2000], presented by *Keen et al.* [1987] (Figure 13a3).

We selected this seismic section because it is perpendicular to the main fault (*Enachescu* [1987, 1988, 1992] and Figure S6 of the supporting information). The overall fault structures look fairly simple over 200 km across the basin, with only one single block in the hanging wall of a major fault, the Murre fault. These cross sections are far from the fault ends (where complications would be expected). Furthermore, the fault trace in map view is also fairly simple, roughly linear.

Withjack and Schlische [2005] have described the rifting evolution between North America and Africa including the formation of the Jeanne d'Arc Basin. *Withjack and Callaway* [2000] have restored the deformations recorded by the Lower and Middle Jurassic (Figures 13a1 and 13a2). Our objective is to apply the sequential limit analysis with a simple prototype geometry and variable sedimentation rates so as to explain the proposed restored deformations. As said above, the main fault of the basin is the Murre fault that bounds the basin to the NW (Figure 13a3). The Murre fault roots in the Moho at 30 km depth [*Keen et al.*, 1987]. We approximate the Murre fault by a piecewise planar fault trace (Figure 13b), whose lower part dips by 18°, according to *Deemer et al.*, 2009 [their Figure 2], who inferred that angle from a migrated seismic reflection line near the 85-4A line of interest here. The dip of the segment *CG* (Figure 13c) is approximately 62° based on the seismic data. The transition between the two planar parts of the Murre fault is chosen at the base of the tilted block (*BCG*) seen in Figure 13a3 at 4.6 s. We estimate this depth at about 13 km below the current sea floor based on
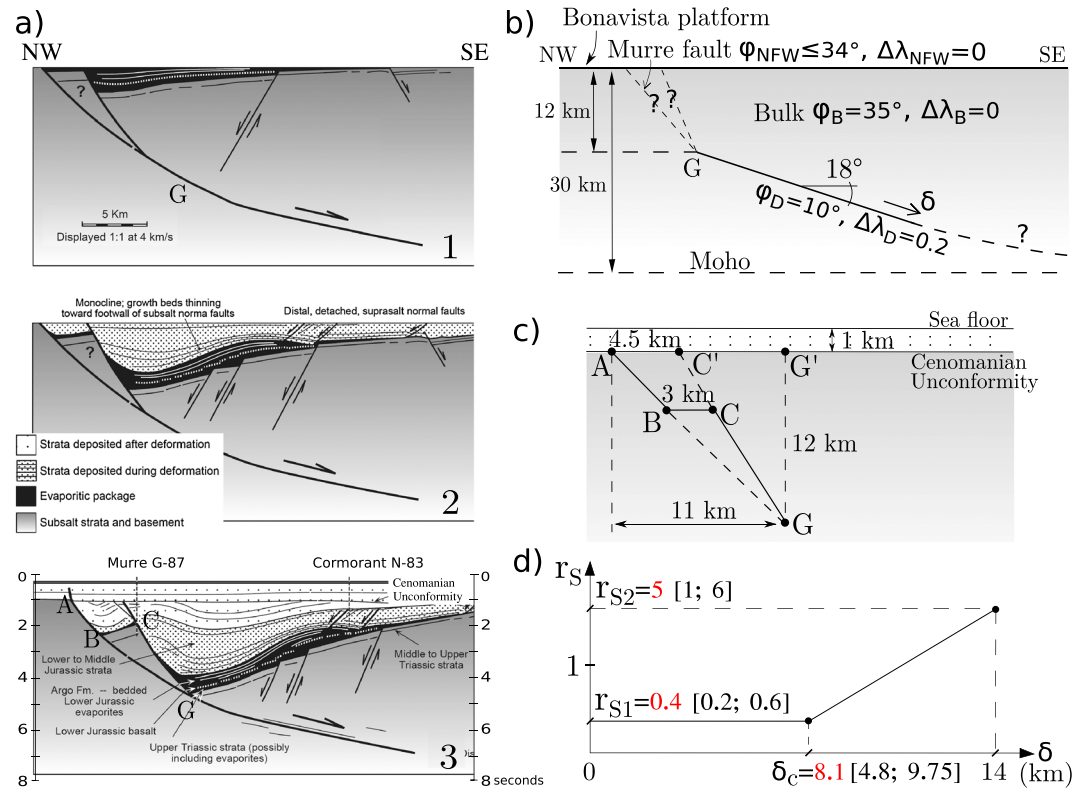
Figure 13. Cross section through the Southern Jeanne d'Arc Basin, Grand Banks, offshore Newfoundland [*Withjack and Callaway*, 2000]. (a) The restorations to the Lower and Middle Jurassic and the interpretation of seismic section 85-4A. (b and c) The geometric idealization used in the limit analysis calculations. Properties of the bulk material, the detachment, and the normal fault with weakening are characterized by the pressure ratio λ_a and the friction angle φ_a (with $a = B, D$, NFW, respectively). (d) The proposed sedimentation ratio r_S is function of the fault displacement δ. The optimized value is in red, and the interval of search is between brackets.

the seismic data of *Deemer et al.* [2009]. This defines the point G which is the root of the FHW structure that is presented in Figures 13b and 13c. The top part (AG) of the Murre fault intersects the Cenomanian unconformity at 11 km from the apex of the G point (distance between A and G'). The initial position of the normal fault corresponds to segment CG, and its position with respect to the Murre fault is based on a 4.5 km estimate of the segment AC' length. Segment BC, assumed horizontal, is 3 km long. The total displacement which takes place on both faults (AB and CG) is the sum of their offsets, estimated at 14 km.

Material properties used for this prototype are summarized in Table 2. The bulk friction angle is set to a constant value of 35°, a typical value for crustal rocks. The weakening of the normal faults is assumed to be in the range 1°–15° (a range sufficiently large to reproduce the size of the tilted block BCG, according to the parametric studies presented earlier). We consider no fluid overpressure except in the lower part of the Murre fault where the overpressure ratio is set to 0.2 and the friction angle to 10°. The change of overpressure ratio with depth is made to satisfy the observation that the crust is overpressured at depth but not at shallower levels [*Suppe*, 2014]. Note that these two values were selected because we also account for the possibility of a major normal fault cutting the whole crust from the Moho in the SE (equivalent to collapse mechanism 2 in Figure 1a). Setting a higher friction angle, or a lesser overpressure, would make it unlikely for the Murre fault to slip at all. The justification of this is presented with the extensional CCW theory in Figure 6b. Another assumption in our prototype is the evolution of the ratio r_S of sedimentation rate to extension rate. We assume here, for simplicity, that this ratio is constant (r_{S1}) for an extension up to δ_c and then it increases linearly to reach r_{S2} at the final extension $\delta = 14$ km (Figure 13d). We expect r_{S1} less than 1 to create a topographic depression responsible for the formation of the FHW region and r_{S2} greater than 1 to fill up the basin.

The sequential limit analysis method provides a forward scenario for any given set of parameters. The optimal simulation results should reproduce four major features of the fault system observed on the cross section of
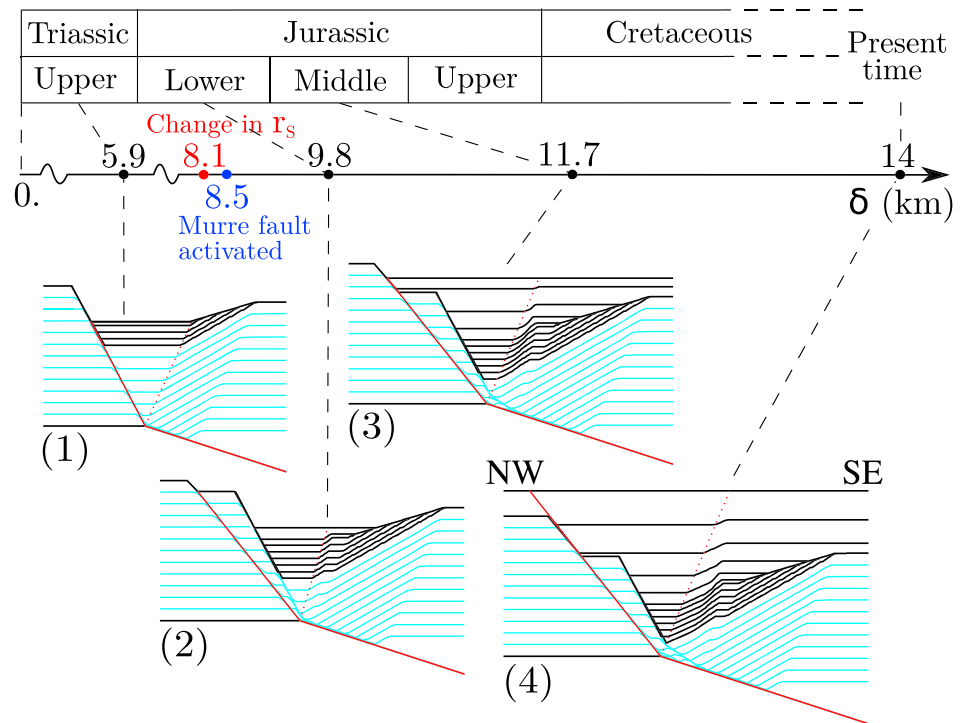
Figure 14. Four steps of the simulation that best fits the four requirements: the order of activation of the bounding faults, the dip of the NW bounding fault, the thickness of the tilted block, and the ratio of offsets on the two bounding faults. Vertical and horizontal scales are equal.

Withjack and Callaway [2000]. First, the fault *CG* was active first and then the Murre fault *AG* to the NW. Second, the segment *BC* should be 3 km long (Figure 13c). Third, the relative amounts of offset on faults *AB* and *CG*, should be, respectively, two thirds and one third, as estimated from Figure 13a3. Lastly, the calculated dip of the Murre fault should be such that the fault intersects the surface at approximately 11 km to the NW of the apex of point *G*.

Our prototype contains many approximations and the following list is certainly far from being complete. We assume a single, continuous extensional tectonic phase. The sediments are considered to be frictional, not compacted and not viscous despite the presence of evaporites in the deformed region and of salt in the hanging wall. Thus, the deformation responsible for the Cormorant anticline is not reproduced. Furthermore, the antithetic faults most likely controlling the position of this anticline are not accounted for in our collapse mechanism. They are replaced at best by axial surfaces with zero offset by definition. Additionally, the model does not consider the block rotation due to the listric shape of the Murre fault. Finally, the history of the sedimentation rate ratio that we adopt is ad hoc. We chose this evolution of the sedimentation ratio with a low constant value switching to a linear increase in order to reproduce first the genesis of the two bounding faults and then the filling up of the basin as seen in the present situation.

The parametric study involves four parameters: $r_{S1}, r_{S2}, \delta_c,$ and the fault friction angle φ_{NFW}. The intervals of search are, respectively, [0.2; 0.6], [1.0; 6.0], [4.8; 9.8] km, and [20°; 34°]. A number of values tested in each range are, respectively, 5, 6, 4, and 15, requiring a total of 1800 simulations. Some simulation results are presented in the supporting information from Figures S7 – S12. In 95% of the cases, the basin is not filled up at the end of the simulation. Among the 90 remaining cases, we eliminated those with more than one tilted block. We choose to present the simulation that reproduces best the four features discussed above (Figure 14). It was obtained with $r_{S1} = 0.4, r_{S2} = 5.0, \delta_c = 8.1$ km, and $\varphi_{NFW} = 25°$.

Our simulation results (numbered 1 to 4 in Figure 14 and denoted YML1 to YML4) and the three sketches in Figure 13a denoted WiCa1 to WiCa3 are now compared. The initial extension occurs most likely in the Upper Triassic, and the normal fault has not yet rotated after a displacement of 5.9 km. The sedimentation rate then starts to increase after a displacement of 8.1 km before the Murre bounding fault is activated at a displacement

of 8.5 km, Figure 14. This activation should occur in the Lower Jurassic such that YML2 corresponds to WiCa1. In the Middle Jurassic, the sedimentation is above the FHW region as seen on YML3 and WiCa2. The sedimentation ratio continues to increase, and the results in YML4 resemble the interpretation in WiCa3, and this is the objective of the whole exercise.

One point deserves some comments. The WaCa2 sketch is not entirely consistent with YML2 predictions: significant subsidence of the depocenter is required to change the activation from the SE of the Murre bounding fault, whereas the proposed restoration WiCa2 considers a filled basin with a flat topography at this time. Our proposed subsidence of the topography in YML2 is about 2.5 km. It is mechanically possible for a material with a cohesion of the order of 10 MPa but is not realistic considering the field observations. The depression depth could be reduced if the growth sediments have a lower density than that of pregrowth sediments (there is lighter salt, for example). The introduction of surface erosion presented in the previous section will not change the main predictions, and thus, we keep with a more probable seafloor geometry at that time. However, the fault offset is preserved in WiCa2 because of the sedimentation, and thus, this surface process is most unlikely to occur.

6. Conclusion

The sequential limit analysis has been applied to capture the 2-D evolution of deformation associated with normal faulting in a tectonic extensional context. This method provides simple means to combine mechanics with a geometrical construction of the geological structure [*Suppe*, 1983]. The half-graben geometrical construction proposed by *Groshong* [1989] defines, in its incremental form, a collapse mechanism appropriate for limit analysis. The method consists of a two-step scheme at each extensional increment. In the first step, the main features of the collapse mechanism (dips of the normal fault and of the axial surface, and position of their common root) are determined according to the kinematic approach of limit analysis [*Yuan et al.*, 2015]. In the second step, the geometry of the structure is updated according to the half-graben kinematics [*Xiao and Suppe*, 1992]. The method can be applied to real topographic profiles. It accounts for material weakening on normal faults, erosion and sedimentation processes, and fluid overpressure. The materials are assumed frictional and cohesive. Elastic or viscous strains are disregarded. The calculations are semianalytical, requiring only a discretization of the topography and moderate numerical implementation.

The sequential limit analysis approach was applied to a wedge of material with a horizontal topography resting on a planar inclined detachment ending with a vertical back wall on its deep side. The retreat of the back wall leads either to a tectonic extensional collapse or to a gravitational collapse [*Yuan et al.*, 2015]. During tectonic collapse, the whole topography is modified to attain a new critical shape well predicted by the Critical Coulomb Wedge (CCW) theory [*Xiao et al.*, 1991], and such that the whole wedge slides on the detachment fault without further internal deformation. During gravitational collapse, the back wall separates from the wedge, which develops a secondary landward, topographic slope well predicted by *Dahlen* [1984]. Increasing the detachment overpressure ratio leads to a transition from a gravitational collapse to a tectonic extensional collapse. The observed surface slopes of the wedge once stable with fluid overpressure on the detachment are well reproduced by the exact CCW theory [*Yuan et al.*, 2015]. The internal deformation bringing the wedge to a stable state is organized in a series of half-grabens. The distribution and positions of the half-graben roots on the detachment during extension have a pattern reminiscent of the findings of *Mary et al.* [2013a, 2013b] in a compressive context.

We considered next the deformation of the cover above a blind detachment fault during extension. The normal fault and the associated active axial surface rotate progressively with applied slip on the detachment. The continuous rotation of the normal fault creates a zone of intense shear of material which passes from the footwall to the hanging wall (FHW region). The rotation of the active axial surface perturbs the folding in the rollover. Fault weakening renders the rotation discontinuous, and the FHW regions are now containing fault-bounded blocks. The formation of FHW regions and their blocky internal structure is observed, at least in analogue experiments using sand [*Dahl*, 1987; *Egholm et al.*, 2007]. Sedimentation reduces the rotations of the normal fault and of the active axial surface, probably because it compensates the subsidence of the hanging wall. There is thus a competition between fault weakening and sedimentation effects in terms of numbers of blocks found in the FHW regions. The sedimentation ratio (defined as the sedimentation rate divided by the vertical component of the slip rate on the normal fault) has to be smaller than 0.6 for the FHW to be observed, and the frictional weakening should not exceed 2° to find at least two blocks in the FHW.

The field application concerns the Southern Jeanne d'Arc Basin, Grand Banks, offshore Newfoundland. We focus on the interpretation of *Withjack and Callaway* [2000] of the seismic line 85-4A and on their proposed restoration. The main structural feature of the interpretation is a FHW region composed of a single block. This requires fault weakening and topographic subsidence in the early part of the rifting. Sedimentation is clearly observed and is accounted for by increasing linearly the sedimentation ratio after an early period at a small constant value. Fault friction and sedimentation parameters are optimized after multiple sequential limit analysis calculations with the objective of matching several features: the timing of the FHW bounding faults, their positions and dips, and the ratio of displacement on the two bounding faults. This inverse-like approach leads us to the conclusion that a deep graben developed in the Lower Jurassic, a conclusion that could be argued by sedimentologists.

Application of sequential limit analysis to regions of normal faulting could be improved in at least three ways. First, normal faults are commonly listric and they were here approximated as bilinear. The listricity of a fault results either from a deformation of the footwall [*Martel*, 2004; *Grasemann et al.*, 2005], a gradual growth during sedimentation, or a change with depth of the fluid pressure conditions [*Mandl and Crans*, 1981]. Second, the half-graben geometry has to be complemented to capture the antithetic faults which are important for oil industry applications as in the Jeanne d'Arc Basin. Third, the ductile response of shales and evaporites should be accounted for, as indicated by laboratory experiments [*Withjack et al.*, 1995; *Withjack and Callaway*, 2000], a difficult task in the framework of limit analysis.

References

Abe, S., H. van Gent, and J. L. Urai (2011), DEM simulation of normal faults in cohesive materials, *Tectonophysics*, *512*(1–4), 12–21.

Anderson, R., M. Zoback, and G. Thompson (1983), Implications of selected subsurface data on the structural form and evolution of some basins in the northern Basin and Range province, Nevada and Utah, *Geol. Soc. Am. Bull.*, *94*(9), 1055–1072.

Chen, W. F. (1975), *Limit Analysis and Soil Plasticity*, Elsevier, Amsterdam.

Cubas, N., Y. M. Leroy, and B. Maillot (2008), Prediction of thrusting sequences in accretionary wedges, *J. Geophys. Res.*, *113*(B12), 1–21.

Cubas, N., C. Barnes, and B. Maillot (2013), Inverse method applied to a sand wedge: Estimation of friction parameters and uncertainty analysis, *J. Struct. Geol.*, *55*, 101–113.

Dahl, N. (1987), Eksperimentelle ekstensjonsbrudd i sand som følge av verticale basementbevegelser: Univ. of Aarhus, Aarhus, Denmark.

Dahlen, F. A. (1984), Noncohesive critical Coulomb wedges: An exact solution, *J. Geophys. Res.*, *89*(B12), 10,125–10,133.

Deemer, S., J. Hall, K. Solvason, K. H. Lau, K. Louden, S. Srivastava, and J.-C. Sibuet (2009), Structure and development of the southeast Newfoundland continental passive margin: Derived from screech transect 3, *Geophys. J. Int.*, *178*(2), 1004–1020.

Egholm, D. L., M. Sandiford, O. R. Clausen, and S. B. Nielsen (2007), A new strategy for discrete element numerical models: 2. Sandbox applications, *J. Geophys. Res.*, *112*, 1–12.

Enachescu, M. (1987), Tectonics and structural framework of the northeast Newfoundland continental margin, in *Sedimentary Basins and Basin-Forming Mechanisms*, vol. 12, edited by C. Beaumont and A. J. Tankard, pp. 117–146, Canadian Society of Petroleum Geologists, Memoir.

Enachescu, M. E. (1988), Extended basement beneath the intracratonic rifted basins of the Grand Banks of Newfoundland, *Can. J. Explor. Geophys.*, *24*(1), 48–65.

Enachescu, M. E. (1992), Enigmatic basins offshore Newfoundland, *Can. J. Explor. Geophys.*, *28*(1), 44–61.

Exadaktylos, G., I. Vardoulakis, M. Stavropoulou, and P. Tsombos (2003), Analogue and numerical modeling of normal fault patterns produced due to slip along a detachment zone, *Tectonophysics*, *376*(1–2), 117–134.

Grasemann, B., S. Martel, and C. Passchier (2005), Reverse and normal drag along a fault, *J. Struct. Geol.*, *27*(6), 999–1010.

Groshong, R. H. (1989), Half-graben structures: Balanced models of extensional fault-bend folds, *Geol. Soc. Am. Bull.*, *101*(1), 96–105.

Holland, M., J. L. Urai, and S. Martel (2006), The internal structure of fault zones in basaltic sequences, *Earth Planet. Sci. Lett.*, *248*(1–2), 301–315.

Keen, C., R. Boutilier, B. De Voogd, B. Mudford, and M. Enachescu (1987), Crustal geometry and extensional models for the Grand Banks, eastern Canada: Constraints from deep seismic reflection data, in *Sedimentary Basins and Basin-Forming Mechanisms*, vol. 12, edited by C. Beaumont and A. J. Tankard, pp. 101–115, Canadian Society of Petroleum Geologists, Memoir.

Lohrmann, J., N. Kukowski, J. Adam, and O. Oncken (2003), The impact of analogue material properties on the geometry, kinematics, and dynamics of convergent sand wedges, *J. Struct. Geol.*, *25*(10), 1691–1711.

Maillot, B., and Y. M. Leroy (2006), Kink-fold onset and development based on the maximum strength theorem, *J. Mech. Phys. Solids*, *54*(10), 2030–2059.

Maillot, B. (2013), A sedimentation device to produce uniform sand packs, *Tectonophysics*, *593*, 85–94.

Mandl, G., and W. Crans (1981), Gravitational gliding in deltas, *Geol. Soc. London Spec. Publ.*, *9*, 41–54.

Marshall, S. T., S. A. Kattenhorn, and M. L. Cooke (2010), Secondary normal faulting in the lake mead fault system and implications for regional fault mechanics, *Geol. Soc. Am. Spec. Pap.*, *463*, 289–310.

Martel, S. (2004), Mechanics of landslide initiation as a shear fracture phenomenon, *Marine Geology*, *203*(3), 319–339.

Mary, B., B. Maillot, and Y. M. Leroy (2013a), Deterministic chaos in frictional wedges revealed by convergence analysis, *Int. J. Numer. Anal. Methods Geomech.*, *37*(17), 3036–3051, doi:10.1002/nag.2177.

Mary, B., B. Maillot, and Y. M. Leroy (2013b), Predicting orogenic wedge styles as a function of analogue erosion law and material softening, *Geochem. Geophys. Geosyst.*, *14*, 4523–4543, doi:10.1002/ggge.20262.

Panien, M., G. Schreurs, and A. Pfiffner (2006), Mechanical behaviour of granular materials used in analogue modelling: Insights from grain characterisation, ring-shear tests and analogue experiments, *J. Struct. Geol.*, *28*(9), 1710–1724, doi:10.1016/j.jsg.2006.05.004.

Pashin, J., and R. Groshong (1998), Structural control of coalbed methane production in Alabama, *Int. J. Coal Geol.*, *38*(1–2), 89–113.

Pons, A., and Y. M. Leroy (2012), Stability of accretionary wedges based on the maximum strength theorem for fluid-saturated porous media, *J. Mech. Phys. Solids*, *60*, 643–664.

Rigo, A., H. LyonCaen, R. Armijo, A. Deschamps, D. Hatzfeld, K. Makropoulos, P. Papadimitriou, and I. Kassaras (1996), A microseismic study in the western part of the Gulf of Corinth (Greece): Implications for large-scale normal faulting mechanisms, *Geophys. J. Int.*, *126*(3), 663–688.

Russell, L., and S. Snelson (1994), Structure and tectonics of the Albuquerque Basin segment of the Rio Grande rift: Insights from reflection seismic data, *Geol. Soc. Am. Spec. Pap.*, *291*, 83–112.

Salençon, J (1974), *Théorie de la plasticité pour les applications à la mécanique des sols*, Eyrolles, Paris.

Salençon, J. (2002), *De l'élasto-plasticité au calcul à la rupture*, École Polytechnique, Palaiseau, and Ellipses, Paris.

Schöpfer, M. P. J., C. Childs, and J. J. Walsh (2007), Two-dimensional distinct element modeling of the structure and growth of normal faults in multilayer sequences: 1. Model calibration, boundary conditions, and selected results, *J. Geophys. Res.*, *112*, B10401, doi:10.1029/2006JB004902.

Suppe, J. (1983), Geometry and kinematics of fault-bend folding, *Am. J. Sci.*, *283*, 684–721.

Suppe, J. (2014), Fluid overpressures and strength of the sedimentary upper crust, *J. Struct. Geol.*, *69*, 481–492.

Tankard, A., H. Welsink, and W. Jenkins (1989), Structural styles and stratigraphy of the Jeanne d'Arc Basin, Grand Banks of Newfoundland, in *Extensional Tectonics and Stratigraphy of the North Atlantic Margins: AAPG Memoir*, vol. 46, pp. 265–282, Am. Assoc. Petrol. Geol., Tulsa, Okla.

Wang, K., J. He, and Y. Hu (2006), A note on pore fluid pressure ratios in the Coulomb wedge theory, *Geophys. Res. Lett.*, *33*, L19310, doi:10.1029/2006GL027233.

Wernicke, B. (1995), Low-angle normal faults and seismicity: A review, *J. Geophys. Res.*, *100*(B10), 20,159–20,174.

Withjack, M., and S. Callaway (2000), Active normal faulting beneath a salt layer: An experimental study of deformation patterns in the cover sequence, *AAPG Bull.*, *84*(5), 627–651.

Withjack, M. O., and R. W. Schlische (2005), A review of tectonic events on the passive margin of eastern North America, in *25th Bob S. Perkins Research Conference: Petroleum Systems of Divergent Continental Margin Basins*, pp. 203–235, Gulf Coast Section of SEPM, Houston, Tex.

Withjack, M. O., Q. T. Islam, and P. R. Lapointe (1995), Normal faults and their hanging-wall deformation—An experimental study, *AAPG Bull.*, *79*(1), 1–18.

Xiao, H.-B., and J. Suppe (1992), Orgin of rollover, *AAPG Bull.*, *76*(4), 509–529.

Xiao, H.-B., F. A. Dahlen, and J. Suppe (1991), Mechanics of extensional wedges, *J. Geophys. Res.*, *96*(B6), 301–318.

Yuan, X. P., Y. M. Leroy, and B. Maillot (2015), Tectonic and gravity extensional collapses in overpressured cohesive and frictional wedges, *J. Geophys. Res. Solid Earth*, *120*, 1833–1854, doi:10.1002/2014JB011612.